

# HypER: Hyperbolic Echo State Networks for Capturing Stretch-and-Fold Dynamics in Chaotic Flows

Pradeep Singh<sup>a,\*</sup>, Sutirtha Ghosh<sup>a,\*\*</sup>, Ashutosh Kumar<sup>a</sup>, Hrishit B P<sup>a</sup> and Balasubramanian Raman<sup>a</sup>

<sup>a</sup>Machine Intelligence Lab, Department of Computer Science and Engineering, IIT Roorkee, India

**Abstract.** Forecasting chaotic dynamics beyond a few Lyapunov times is difficult because infinitesimal errors grow exponentially. Existing Echo State Networks (ESNs) mitigate this growth but employ reservoirs whose Euclidean geometry is mismatched to the *stretch-and-fold* structure of chaos. We introduce the *Hyperbolic Embedding Reservoir* (HypER), an ESN whose neurons are sampled in the Poincaré ball and whose connections decay exponentially with hyperbolic distance. This negative-curvature construction embeds an *exponential metric* directly into the latent space, aligning the reservoir’s local expansion–contraction spectrum with the system’s Lyapunov directions while preserving standard ESN features such as sparsity, leaky integration and spectral-radius control. Training is limited to a Tikhonov-regularised read-out. On the chaotic Lorenz-63 and Rössler systems, and the hyperchaotic Chen–Ueta attractor, HypER consistently lengthens the mean valid-prediction horizon beyond Euclidean and graph-structured ESN baselines, with statistically significant gains confirmed over 30 independent runs; parallel results on real-world benchmarks—including heart-rate variability from the Santa Fe and MIT-BIH datasets, and international sunspot numbers—corroborate its advantage. We further establish a lower bound on the rate of state divergence for HypER, mirroring Lyapunov growth. In the interest of reproducibility, we release our implementation at [github.com/deepdyn/HypER](https://github.com/deepdyn/HypER) and provide a full technical appendix (proofs, ablations, hyperparameters) in the arXiv preprint at DOI: 10.48550/arXiv:XXXX.XXXXX.

## 1 Introduction

Neural circuits in the brain are often conceptualized as high-dimensional dynamical systems that can host *attractor* states—regions in phase space where network activity converges or persists over time—and these attractors underlie vital processes such as working memory, decision-making, and robust perception [13, 38]. Electrophysiological and calcium-imaging evidence further indicates that many cortical microcircuits operate near the edge of chaos, where trajectories explore a rich repertoire of quasi-stable states yet remain exquisitely sensitive to perturbations [2, 27]. Capturing such behaviour is notoriously difficult because any modelling or measurement error is amplified exponentially: if two initial conditions differ by  $\|\delta x_0\|$ , their separation grows on average as  $\|\delta x_t\| \approx \|\delta x_0\| \exp(\lambda_{\max} t)$  wherever the largest Lyapunov exponent (LLE)  $\lambda_{\max}$  is positive. Beyond a few Lyapunov times accurate prediction becomes impossible unless the model itself encodes the

local “stretch-and-fold” geometry that underlies chaotic divergence. From a theoretical standpoint, capturing these highly sensitive, self-organizing phenomena calls for a modeling framework that can explicitly reflect the underlying geometry of exponential separation.

Reservoir computing (RC), and especially Echo State Networks (ESNs), has emerged as a promising data-driven framework for chaos forecasting because it replaces costly recurrent training with a fixed nonlinear reservoir and a linear read-out [14]. ESNs can learn short-term structure and even replicate Lyapunov spectra of benchmark systems, yet the typical prediction horizon remains limited to roughly 5–8 Lyapunov times [9, 17]. A plausible reason is geometric: conventional reservoirs are embedded in flat Euclidean space or simple random graphs and therefore lack an explicit inductive bias for the exponential expansion and contraction intrinsic to chaotic flows.

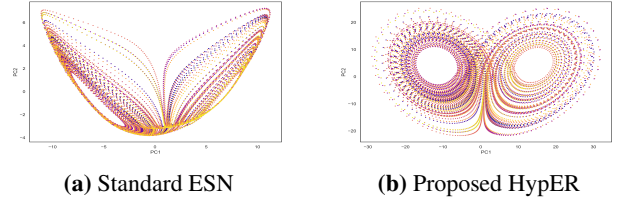


**Figure 1.** Two-dimensional PCA projections of high-dimensional reservoir states (*no read-out training applied*) for (a) a standard ESN and (b) the proposed HypER, when both networks are driven by the Lorenz system.

Hyperbolic spaces with constant negative curvature are characterized by metric properties that mirror exponential growth: distances and volumes expand exponentially with radius, unlike Euclidean spaces where growth is polynomial [42]. Intuitively, a small change in coordinates on a hyperbolic manifold can produce a large change in geodesic distance, akin to how a small state perturbation in a chaotic system leads to a large future divergence. This makes hyperbolic geometry a natural substrate to model the local instabilities of chaos. Yet, most sequential models, bound to flat Euclidean latents, struggle to reproduce this exponential pull—begging a sharper question:

*Does wiring a reservoir in hyperbolic space unlock a longer glimpse into chaotic futures?*

We contend that a negatively curved latent space supplies exactly that bias. In the Poincaré ball model, hyperbolic sampling preserves the natural volume element, so nodes near the boundary correspond to rapidly diverging directions while central nodes capture contracting modes. Empirical tests on the Lorenz–63, Rössler, and Chen–

\* Corresponding Author. Email: [pradeep.cs@src.iitr.ac.in](mailto:pradeep.cs@src.iitr.ac.in)

\*\* Corresponding Author. Email: [s\\_ghosh@cs.iitr.ac.in](mailto:s_ghosh@cs.iitr.ac.in)

Ueta attractors show that a modest-sized Hyper consistently extends the valid-prediction window and slows error growth relative to Euclidean and graph-structured baselines. These results position hyperbolic geometry as a principled lever for long-range prediction in both neuroscience and nonlinear-dynamics applications.

**Summary of Key Contributions.** We present Hyper, the first reservoir computer whose neurons are embedded in the Poincaré ball and whose recurrent weights decay exponentially with hyperbolic distance. This curvature-aware wiring installs an inductive bias missing from Euclidean or graph-structured ESNs and, supported by a state-divergence theorem, translates into substantially longer and more stable forecasts. Empirically, Hyper not only extends the prediction horizon on canonical Lorenz-63, Rössler, Chen-Ueta, and Chua attractors, but also delivers strong multi-step accuracy on real-world chaotic benchmarks—including the Santa Fe Dataset B, MIT-BIH, and international sunspot numbers.

## 2 Background and Related Works

**Chaotic Dynamics and the Limits of Predictability.** A deterministic dynamical system is specified by a flow  $\psi_t : \mathcal{M} \rightarrow \mathcal{M}$  on a smooth manifold  $\mathcal{M}$ ; the state  $\mathbf{x}_t = \psi_t(\mathbf{x}_0)$  evolves according to  $\dot{\mathbf{x}} = F(\mathbf{x})$  in continuous time or  $\mathbf{x}_{k+1} = G(\mathbf{x}_k)$  in discrete time [18]. With initial conditions  $\mathbf{x}_0, \mathbf{y}_0$ , nearby trajectories satisfy  $\|\psi_t(\mathbf{x}_0) - \psi_t(\mathbf{y}_0)\| \simeq \|\mathbf{x}_0 - \mathbf{y}_0\| \exp(\lambda_{\max} t)$ , so they diverge when the largest Lyapunov exponent  $\lambda_{\max} > 0$  (the classical signature of chaos) and converge exponentially when  $\lambda_{\max} < 0$  [8]. The amplification continues until nonlinear folding confines the motion to a *strange attractor*, whose fractal geometry can be visualised through Poincaré sections or return maps—classical examples are the double-scroll Lorenz set and the horseshoe-like Rössler map [23, 37]. Because the forecast error grows by a factor of  $e$  roughly every  $1/\lambda_{\max}$  time units, even perfect models face a finite predictability horizon (about two weeks for mid-latitude weather [31]). Any learning system aimed at long-range forecasting must therefore encode, rather than merely fit, the local stretch-and-fold geometry that drives error growth.

**Reservoir Computing for Chaotic Time Series.** ESNs and their real-time spiking analogue, the Liquid State Machine, sidestep the difficulties of full recurrent training by fixing the recurrent weights of a large, sparsely connected “reservoir” and learning only a linear read-out [14, 25]. When the spectral radius  $\rho(\mathbf{W}) < 1$ , the *Echo-State Property* (ESP) guarantees that all influences of arbitrary initialisation vanish, leaving a fading-memory encoding of recent inputs. But long-horizon chaos prediction pushes the reservoir to the opposite regime: one must drive  $\rho(\mathbf{W})$  towards unity to sustain the internal dynamics, at which point ESP becomes fragile and the model either explodes or collapses. Traditionally tuned closed-loop ESNs achieve only 5–8 Lyapunov times before divergence on Lorenz-63, Kuramoto–Sivashinsky and climate benchmarks [9, 17, 33]. Subsequent variants—small-world, scale-free, even fully *uncoupled* reservoirs—shift the memory-nonlinearity balance but remain *Euclidean*, offering no bias toward the exponential expansion that defines chaos [24, 35]. Hyper remedies this tension by normalising the spectrum after curvature-aware weight construction, raising the *minimum* singular value while keeping  $\rho(\mathbf{W}) < 1$ . The network thus retains ESP yet still magnifies perturbations at a provably super-unit rate, extending prediction horizons without sacrificing stability.

**Hyperbolic Geometry in Machine Learning.** Negative-curvature manifolds accommodate exponential growth in volume, making

them ideal for embedding trees and other hierarchical structures with low distortion. Nickel and Kiela’s Poincaré embeddings [29] sparked a wave of hyperbolic-representation methods, from gyrovector-based feed-forward layers to hyperbolic graph neural networks [4, 11]. These models exploit the fact that a small Euclidean displacement near the boundary of the Poincaré ball corresponds to a large geodesic increment, mirroring the sensitivity required to separate similar objects in hierarchical data. Despite this progress, hyperbolic deep learning has focused almost exclusively on static tasks; we are unaware of prior work that harnesses negative curvature to model *continuous-time chaotic dynamics*. Our Hyper architecture fills that gap by sampling reservoir nodes directly in hyperbolic space and defining connectivity as an exponential function of hyperbolic distance, thereby hard-coding the stretch-and-fold metric into the recurrent state itself.

Taken together, these strands motivate our *central hypothesis*: embedding the reservoir in a Poincaré ball couples the network’s internal geometry to the stretch-fold mechanism of chaos, enabling longer and more stable forecasts than any flat-space or purely graph-based ESN examined to date. Figure 1 illustrates the point. Driven by the same Lorenz signal—and *before* any supervised read-out is trained—the vanilla ESN does reproduce a two-lobe structure, but the lobes are warped and compressed toward the centre; in contrast, Hyper traces two crisp, well-separated wings that closely match the topology of the true attractor.

## 3 Methodology

**Problem Statement.** Let  $\{\mathbf{u}_t\}_{t \in \mathcal{T}} \subset \mathbb{R}^m$  be a time series generated by a chaotic system of dimension  $m$ . Our objective is to construct an ESN that, given a finite training segment  $\{\mathbf{u}_t\}_{t=1}^T$ , learns to forecast  $\mathbf{u}_{t+1} \in \mathbb{R}^m$  in an autoregressive fashion for  $t > T$ . Formally, we seek to minimize the multi-step prediction error  $\sum_{t=T+1}^{T+H} \|\mathbf{u}_t - \hat{\mathbf{u}}_t\|^2$  over some horizon  $H \gg 1$ .

### 3.1 Hyperbolic Embeddings and Adjacency

**Poincaré Ball Model.** Let  $(\mathcal{B}^d, g_\chi)$  be the  $d$ -dimensional Poincaré ball endowed with the Riemannian metric  $g_\chi$  of constant sectional curvature  $\chi < 0$ . For a fixed integer  $d \geq 2$ , the *Poincaré  $d$ -ball* of radius 1 is given by  $\mathcal{B}^d = \{\mathbf{p} \in \mathbb{R}^d \mid \|\mathbf{p}\| < 1\}$ , where  $\|\cdot\|$  denotes the usual Euclidean norm in  $\mathbb{R}^d$ . The geometry in this model is governed by a Riemannian metric [7, 20] given by  $ds^2 = \frac{4 \sum_{i=1}^d dx_i^2}{(1 - \sum_{i=1}^d x_i^2)^2}$ , ensuring that distances grow infinitely large as one approaches the boundary of the model. Distances in this ball are expressed as

$$d_{\mathbb{H}}(\mathbf{p}_i, \mathbf{p}_j) = \operatorname{arcosh} \left( 1 + 2 \frac{\|\mathbf{p}_i - \mathbf{p}_j\|^2}{(1 - \|\mathbf{p}_i\|^2)(1 - \|\mathbf{p}_j\|^2)} \right), \quad (1)$$

where  $\operatorname{arcosh}(\zeta) = \ln(\zeta + \sqrt{\zeta^2 - 1})$ . Geodesics in the Poincaré ball model are either straight lines through the origin or circular arcs that intersect the boundary orthogonally [1]. The model enjoys conformality, meaning that angles are preserved [39], making it particularly valuable for embedding tasks in machine learning where local geometric relationships are important [29].

**Node Placement.** Let  $N$  be the dimension (number of nodes) of the reservoir. To embed these nodes in a  $d$ -dimensional hyperbolic geometry, we assign each node  $i \in \{1, 2, \dots, N\}$  a coordinate  $\mathbf{p}_i \in \mathcal{B}^d$ . A variety of sampling schemes are possible for placing nodes in the Poincaré ball  $\mathcal{B}^d$ . We highlight two distinct strategies, each of which

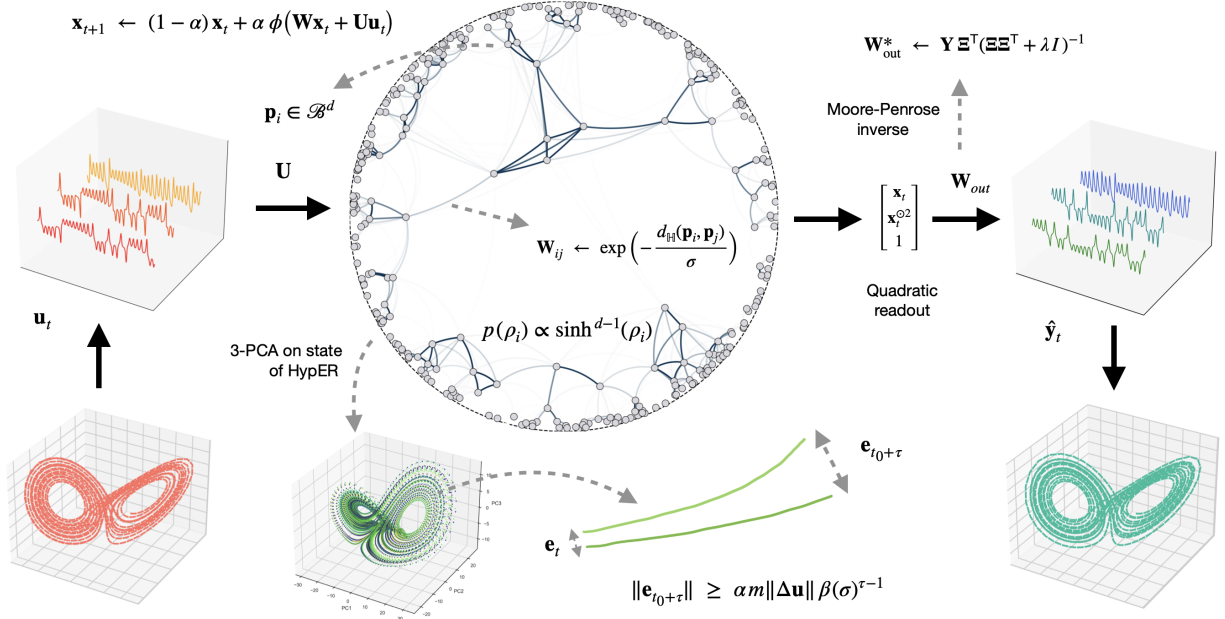


**Figure 2.** HyperER embedded in the Poincaré disk: nodes placed evenly in hyperbolic volume, links decay with distance.

assigns radial and angular coordinates  $(r_i, \omega_i)$  and hence yields a node position  $\mathbf{p}_i = r_i \omega_i$ , where  $r_i = \|\mathbf{p}_i\| < 1$  is the magnitude of  $\mathbf{p}_i$  and  $\omega_i \in \mathbb{S}^{d-1}$  is a unit vector on the  $(d-1)$ -dimensional sphere, representing the direction. The open-ball constraint  $\|\mathbf{p}_i\| < 1$  guarantees that the hyperbolic distance (refer Eqn. 1) is well-defined.

(i) *Euclidean-Isotropic Sampling (Baseline)*: In this scheme, we do not take into account the hyperbolic distance distribution when choosing  $r_i$  and instead sample it to be uniformly distributed according to the Euclidean volume in the ball of radius  $R < 1$ . Concretely, we set  $r_i = \sqrt[d]{u_i} R$  where  $u_i \sim \text{Uniform}(0, 1)$ . Then, the direction  $\omega_i \in \mathbb{S}^{d-1}$  is sampled uniformly on the  $(d-1)$ -dimensional sphere, owing to the symmetry of the Poincaré ball. However, this method does *not* produce a uniform distribution with respect to the hyperbolic volume element, and nodes closer to the boundary will not reflect the exponential concentration that true hyperbolic geometry would suggest. We include it as a baseline for ablation studies (cf. §4), to compare how a purely Euclidean-based distribution affects performance relative to a geometry-aware distribution.

(ii) *Hyperbolic-Uniform Sampling*: For a full match to the negative-curvature volume element, we let the hyperbolic radius  $\rho_i \in [0, \rho_{\max}]$  be distributed according to the probability density function (PDF)  $p(\rho_i) \propto \sinh^{d-1}(\rho_i)$ , where  $\rho_i = 2 \operatorname{artanh}(r_i)$  in the Poincaré model. After sampling  $\rho_i$ , we then convert it to its Euclidean counterpart  $r_i = \tanh(\frac{\rho_i}{2})$  and again draw the angular components  $\omega_i$  uniformly on  $\mathbb{S}^{d-1}$ . Focusing on the case of the Poincaré disc, the PDF takes the form  $p(\rho_i) \propto \sinh(\rho_i)$ . It is straightforward to obtain the cumulative distribution function (CDF)  $F(\rho_i) = \int_0^{\rho_i} p(\rho) d\rho \propto \cosh(\rho_i) - 1$ . Equating the normalized CDF to  $u_i \sim \text{Uniform}(0, 1)$  guarantees that the samples are uniformly distributed in probability space

$$\frac{F(\rho_i)}{F(\rho_{\max})} = \frac{\cosh(\rho_i) - 1}{\cosh(\rho_{\max}) - 1} = u_i. \quad (2)$$

Accordingly, we obtain the hyperbolic radius  $\rho_i$  as follows  $\rho_i = \operatorname{arcosh}(u_i(\cosh(\rho_{\max}) - 1) + 1)$ . This procedure is precisely uniform with respect to the hyperbolic volume element in a  $d$ -

dimensional space of constant curvature  $-1$ . Consequently, it generates point placements that reflect the genuine exponential “stretching” near the boundary  $\|\mathbf{p}_i\| \rightarrow 1$ . In applications where it is crucial to respect the native hyperbolic measure, this approach is the most principled choice [1]. Note that both sampling schemes satisfy  $\|\mathbf{p}_i\| < 1$  by construction, and yield valid embeddings in the Poincaré ball for which the hyperbolic distance (Eqn. 1) is well-defined.

**Connectivity Kernel.** For any pair of nodes  $i$  and  $j$ , we compute their hyperbolic distance  $d_H(\mathbf{p}_i, \mathbf{p}_j)$ . We define the reservoir’s adjacency matrix by applying an exponential kernel to the hyperbolic metric  $W_{ij} = \exp\left(-\frac{d_H(\mathbf{p}_i, \mathbf{p}_j)}{\sigma}\right)$ , for  $1 \leq i, j \leq N$ , where  $\sigma > 0$  is the *kernel width* controlling how rapidly connectivity decays with increasing hyperbolic distance. Concretely, two nodes that lie close enough in  $\mathcal{B}^d$  (i.e.,  $\mathbf{p}_i \approx \mathbf{p}_j$ ) will have relatively large weight  $W_{ij}$ , whereas nodes far apart in hyperbolic distance will be coupled only weakly (or nearly zero if we impose sparsity conditions) (cf. Figure 2). Consequently,  $W$  reflects the geometry of negative curvature: nodes near the boundary can have large pairwise distances and, thus, smaller mutual connection strengths.

**Lemma 1** (Spectrum of the hyperbolic kernel). *Let  $\{\mathbf{p}_i\}_{i=1}^N \subset \mathcal{B}^d$  be distinct points. Set  $\delta = \min_{i \neq j} d_H(\mathbf{p}_i, \mathbf{p}_j)$ . Then  $\lambda_{\min}(\mathbf{W}) \geq 1 - (N-1)e^{-\delta/\sigma}$ ,  $\rho(\mathbf{W}) \leq 1 + (N-1)e^{-\delta/\sigma}$ . (Proof in supplementary)*

**Sparsity & Spectral Normalization.** For computational efficiency and enhanced dynamical properties, we impose *row-level sparsity* on  $W$ . For each row  $i \in \{1, \dots, N\}$ , we keep only the top- $\kappa$  largest entries of row  $i$  and set all others to zero. Denote the resulting sparse matrix by  $\tilde{\mathbf{W}}$ . We then ensure that the reservoir’s internal dynamics satisfy the ESP [14] by restricting the spectral radius of  $\tilde{\mathbf{W}}$ . Define the final reservoir matrix  $\mathbf{W} \in \mathbb{R}^{N \times N}$  as  $\frac{\varrho}{\rho(\tilde{\mathbf{W}})} \tilde{\mathbf{W}}$ , where  $\rho(\tilde{\mathbf{W}})$

denotes the spectral radius of  $\tilde{\mathbf{W}}$ , and  $\varrho \in (0, 1)$  is a user-specified target radius. This *spectral normalization* preserves the geometry-induced pattern in  $\tilde{\mathbf{W}}$  while ensuring that repeated application of  $\mathbf{W}$  does not drive unbounded state growth. By choosing  $\varrho < 1$ , we allow

the reservoir to possess sufficiently rich dynamics near the edge of stability while still converging during teacher forcing.

### 3.2 Reservoir Configuration

**Leaky Echo State Update.** The reservoir is modeled as a discrete-time recurrence relation with a state-space representation. Recall that  $\mathbf{u}_t \in \mathbb{R}^m$  denotes the input at time  $t$  and define  $\mathbf{x}_t \in \mathbb{R}^N$  as the reservoir state vector at time  $t$ . The dynamical evolution of the *leaky ESN* is given by the state update equation

$$\mathbf{x}_{t+1} = (1 - \alpha) \mathbf{x}_t + \alpha \phi(\mathbf{W} \mathbf{x}_t + \mathbf{U} \mathbf{u}_t), \quad (3)$$

where  $\alpha \in (0, 1]$  is the *leak rate*,  $\mathbf{U} \in \mathbb{R}^{N \times m}$  is a random *input weight* matrix, and  $\phi: \mathbb{R}^N \rightarrow \mathbb{R}^N$  is a 1-Lipschitz pointwise nonlinear activation. The term  $(1 - \alpha)\mathbf{x}_t$  provides a leaky integration that can enhance memory and stability in the reservoir [14, 15].

**Lemma 2** (Linearized forward sensitivity). *Let  $\mathbf{W} \in \mathbb{R}^{N \times N}$  be symmetric; denote its smallest eigenvalue by  $\lambda_{\min}(\mathbf{W}) \geq 0$ ; the activation  $\phi$  is  $C^1$  with derivative bounded on the reachable domain by  $0 < m \leq \phi'(z) \leq L < \infty$ . For any current input  $u$  and reservoir state  $x$  define  $J(\mathbf{x}) = \frac{\partial \mathbf{x}_{t+1}}{\partial \mathbf{x}_t} = (1 - \alpha)I + \alpha D_\phi(\mathbf{x}) \mathbf{W}$ , where  $D_\phi(\mathbf{x}) = \text{diag}(\phi'(\mathbf{W}\mathbf{x} + \mathbf{U}\mathbf{u}))$ . Then  $s_{\min}(J(\mathbf{x})) \geq \sqrt{\frac{m}{L}}[(1 - \alpha) + \alpha m \lambda_{\min}(\mathbf{W})]$  and  $\|J(\mathbf{x})\| \leq \sqrt{\frac{L}{m}}[(1 - \alpha) + \alpha L \rho(\mathbf{W})]$ . (Proof in supplementary)*

**Theorem 3** (State-divergence lower bound). *Let  $\phi$  be twice differentiable, monotone, and strictly bounded:  $0 < m \leq \phi'(z) \leq L$  on the reachable domain. Define*

$$\beta(\sigma) := \sqrt{\frac{m}{L}}[(1 - \alpha) + \alpha m \varrho \frac{\lambda_{\min}(\mathbf{W}(\sigma))}{\rho(\mathbf{W}(\sigma))}] \quad (4)$$

*Let two input streams coincide up to time  $t_0 - 1$ , differ at  $t_0$  ( $\mathbf{u}_{t_0} \neq \mathbf{v}_{t_0}$ ), and coincide thereafter. For the resulting reservoir trajectories  $\mathbf{x}_t, \mathbf{y}_t$  put  $\mathbf{e}_t := \mathbf{x}_t - \mathbf{y}_t$  and set  $\Delta \mathbf{u} := \mathbf{U}(\mathbf{u}_{t_0} - \mathbf{v}_{t_0}) \neq 0$ . If  $\beta(\sigma) > 1$ , then for every integer  $\tau \geq 1$ ,  $\|\mathbf{e}_{t_0+\tau}\| \geq \alpha m \|\Delta \mathbf{u}\| \beta(\sigma)^{\tau-1}$ .*

*Proof.* For the initial error injection at  $t_0$ , because the inputs agree up to  $t_0 - 1$  we have  $\mathbf{e}_{t_0} = 0$ . At  $t_0$ ,  $\mathbf{e}_{t_0+1} = (1 - \alpha)\mathbf{e}_{t_0} + \alpha[\phi(\mathbf{W}\mathbf{x}_{t_0} + \mathbf{U}\mathbf{u}_{t_0}) - \phi(\mathbf{W}\mathbf{x}_{t_0} + \mathbf{U}\mathbf{v}_{t_0})]$ , and the mean-value theorem plus  $\phi' \geq m$  yields  $\|\mathbf{e}_{t_0+1}\| \geq \alpha m \|\Delta \mathbf{u}\|$  with  $\Delta \mathbf{u} := \mathbf{U}(\mathbf{u}_{t_0} - \mathbf{v}_{t_0})$ .

For propagation for  $\tau \geq 2$ ,  $\mathbf{e}_{t_0+\tau} = J(\xi_{t_0+\tau-1}) \mathbf{e}_{t_0+\tau-1}$ , where  $\xi_t$  lies on the segment between  $\mathbf{x}_t$  and  $\mathbf{y}_t$ . Invoking the lower singular-value bound in Lemma 2 gives  $\|\mathbf{e}_{t_0+\tau}\| \geq \beta(\sigma) \|\mathbf{e}_{t_0+\tau-1}\|$ . Iterating and bootstrapping yields  $\|\mathbf{e}_{t_0+\tau}\| \geq \alpha m \|\Delta \mathbf{u}\| \beta(\sigma)^{\tau-1}$ . Ensuring  $\beta(\sigma) > 1$ , and combining with (4) gives  $\beta(\sigma) \geq \sqrt{\frac{m}{L}}[(1 - \alpha) + \alpha m \varrho \frac{1 - (N-1)e^{-\delta/\sigma}}{1 + (N-1)e^{-\delta/\sigma}}]$ . For fixed  $m, L, \alpha, \varrho$  this expression is strictly increasing as  $\sigma \downarrow 0$  because the fraction inside the brackets rises to 1. Thus one can always pick a kernel width  $\sigma > 0$  small enough that  $\beta(\sigma) > 1$ , guaranteeing exponential separation while the spectral normalisation  $\varrho$  keeps the echo-state property intact. Ergo, one can always choose  $\sigma$  small enough (yet positive) so that  $\beta(\sigma) > 1$ ; the kernel width thus becomes a tunable knob controlling the guaranteed expansion.  $\square$

Theorem 3 crystallises HypER’s intuition: a hyperbolic kernel with width  $\sigma$  and subsequent spectral rescale to  $\varrho < 1$  yields a Jacobian whose worst-case gain is  $s_{\min}(J(\mathbf{x})) \geq \beta(\sigma) = \sqrt{m/L}[(1 -$

---

#### Algorithm 1: HYPER Construction

---

**Require:** reservoir size  $N$ , manifold dimension  $d > 1$ , kernel width  $\sigma$ , sparsity level  $\kappa$ , target spectral radius  $\varrho < 1$

**Ensure:** sparse, spectrally-normalised adjacency matrix  $\mathbf{W} \in \mathbb{R}^{N \times N}$

```

1: // Hyperbolic node sampling
2: for  $i \leftarrow 1$  to  $N$  do
3:   draw  $u_i \sim \mathcal{U}(0, 1)$  {inverse-CDF for uniform hyperbolic volume}
4:    $\rho_i \leftarrow \text{arcosh}(u_i (\cosh \rho_{\max}) - u_i + 1)$ 
5:    $r_i \leftarrow \tanh(\rho_i/2)$ 
6:   sample  $\omega_i \in \mathbb{S}^{d-1}$  uniformly
7:    $\mathbf{p}_i \leftarrow r_i \omega_i$  {node position in  $\mathcal{B}^d$ }
8: end for
9: // Geometry-aware weight kernel
10: for all  $(i, j) \in \{1, \dots, N\}^2$  do
11:    $d_{ij} \leftarrow \text{arcosh}(1 + 2 \frac{\|\mathbf{p}_i - \mathbf{p}_j\|^2}{(1 - \|\mathbf{p}_i\|^2)(1 - \|\mathbf{p}_j\|^2)})$ 
12:    $W_{ij} \leftarrow \exp(-d_{ij}/\sigma)$ 
13: end for
14: // Row-wise sparsification
15: for  $i \leftarrow 1$  to  $N$  do
16:   keep the  $\kappa$  largest entries in row  $i$  of  $\mathbf{W}$ ; set others to 0
17: end for
18: // Spectral normalisation to satisfy ESP
19:  $\rho \leftarrow$  largest eigenvalue modulus of  $\mathbf{W}$ 
20:  $\mathbf{W} \leftarrow (\varrho/\rho) \mathbf{W}$ 
21: return  $\mathbf{W}$ 

```

---

$\alpha) + \alpha m \varrho \lambda_{\min}(\mathbf{W})/\rho(\mathbf{W})]$ . Because  $\lambda_{\min}(\mathbf{W})/\rho(\mathbf{W})$  grows exponentially as  $\sigma \downarrow 0$  in the Poincaré ball, one can always push  $\beta(\sigma) > 1$ ; every infinitesimal perturbation is then amplified, faithfully reflecting the positive Lyapunov exponent of chaotic flows, yet global stability is preserved by the same  $\varrho$  that enforces the echo-state property. In Euclidean reservoirs this ratio shrinks polynomially with size, forcing  $\beta(\sigma) \leq 1$  and thus damping, not stretching, differences. The bound also uncovers how node non-linearities condition expansion through the factor  $\sqrt{m/L}$ : a heterogeneous palette broadens the reservoir’s functional basis only when  $\beta(\sigma) > 1$ ; otherwise their contributions vanish or destabilise the network. Hyperbolic connectivity therefore supplies the sole geometry that simultaneously guarantees per-step expansion, respects ESP, and lets diverse activations add predictive power, explaining why mixed non-linearities help HypER yet hurt or do nothing for flat-geometry ESNs.

**Polynomial Readout.** Following standard ESN methodology, we *train* only an output layer that maps  $\mathbf{x}_t$  to the next state  $\mathbf{u}_{t+1}$ . During training, the input signal  $\{\mathbf{u}_t\}_{t=1}^T$  is fed into the reservoir and the corresponding reservoir states  $\{\mathbf{x}_t\}_{t=T_w+1}^T$  are recorded after the washout. We adopt a polynomial expansion for the readout  $\xi_t = [x_t^1, \dots, x_t^N, (x_t^1)^2, \dots, (x_t^N)^2, 1]^T$ , where the squared terms add a limited second-order nonlinearity, and the constant 1 term captures any bias [3, 30]. Hence,  $\xi_t \in \mathbb{R}^{2N+1}$  and the readout matrix  $\mathbf{W}_{\text{out}} \in \mathbb{R}^{m \times (2N+1)}$ . The single-step-ahead predicted output is expressed as  $\hat{\mathbf{u}}_{t+1} = \mathbf{W}_{\text{out}} \xi_t$ . After collecting  $\{\xi_t, \mathbf{u}_{t+1}\}$  for  $t = T_w + 1, \dots, T$ , we solve the *ridge regression* problem  $\min_{\mathbf{W}_{\text{out}}} \sum_{t=T_w+1}^T \|\mathbf{u}_{t+1} - \mathbf{W}_{\text{out}} \xi_t\|^2 + \lambda \|\mathbf{W}_{\text{out}}\|_F^2$ , where  $\|\cdot\|_F$  denotes the Frobenius norm, and  $\lambda > 0$  is the  $L_2$ -regularization coefficient. The closed-form analytical solution for the ridge regression yields  $\mathbf{W}_{\text{out}}^* = \mathbf{Y} \Xi^T (\Xi \Xi^T + \lambda I)^{-1}$ , where  $\mathbf{Y}$  stacks the



**Table 1.** NRMSE for autoregressive forecasting across multiple prediction horizons on canonical chaotic benchmarks.

Dataset	Horizon	NRMSE ↓						
		ESN	SCR	CRJ	SW-ESN	MCI-ESN	DeepESN	HypER
Lorenz	200	0.1050 ± 0.1586	0.1061 ± 0.2249	0.0494 ± 0.0243	0.0224 ± 0.0143	0.0035 ± 0.0026	0.2746 ± 0.4853	<b>0.0002 ± 0.0001</b>
	400	1.1795 ± 0.3572	1.1718 ± 0.6335	0.9309 ± 0.2552	0.6417 ± 0.2895	0.3086 ± 0.3725	1.2616 ± 0.4225	<b>0.0124 ± 0.0104</b>
	600	1.7705 ± 0.2058	1.9862 ± 0.9876	1.6462 ± 0.1888	1.4118 ± 0.3359	0.8031 ± 0.4980	1.7473 ± 0.2495	<b>0.0483 ± 0.0414</b>
	800	1.9840 ± 0.1512	2.3832 ± 1.2483	1.8971 ± 0.2022	1.7489 ± 0.2176	1.4190 ± 0.2962	1.9723 ± 0.1619	<b>0.8865 ± 0.2899</b>
	1000	2.1093 ± 0.2033	2.5817 ± 1.4351	2.0490 ± 0.3540	1.8956 ± 0.2003	1.6795 ± 0.2205	2.0663 ± 0.1326	<b>1.2580 ± 0.2721</b>
Rössler	200	0.0036 ± 0.0006	0.0053 ± 0.0023	0.0066 ± 0.0023	0.0063 ± 0.0015	0.0038 ± 0.0017	0.0059 ± 0.0010	<b>0.0007 ± 0.0003</b>
	400	0.0637 ± 0.1875	0.0664 ± 0.1317	0.0319 ± 0.0250	0.0289 ± 0.0215	0.0083 ± 0.0042	0.0374 ± 0.0341	<b>0.0019 ± 0.0008</b>
	600	0.0936 ± 0.2846	0.1222 ± 0.2882	0.0481 ± 0.0387	0.0470 ± 0.0364	0.0113 ± 0.0064	0.0542 ± 0.0583	<b>0.0024 ± 0.0010</b>
	800	0.1603 ± 0.4714	0.2134 ± 0.5601	0.0629 ± 0.0486	0.0700 ± 0.0574	0.0194 ± 0.0245	0.0735 ± 0.0911	<b>0.0033 ± 0.0014</b>
	1000	0.1963 ± 0.5000	0.2494 ± 0.4606	0.0812 ± 0.0499	0.0932 ± 0.0830	0.0312 ± 0.0509	0.1095 ± 0.1243	<b>0.0061 ± 0.0031</b>
Chen-Ueta	200	1.6613 ± 0.7941	1.6366 ± 0.4114	1.6308 ± 1.0914	1.5562 ± 0.2400	1.1049 ± 0.3810	1.8560 ± 0.5049	<b>0.0259 ± 0.0244</b>
	400	2.3164 ± 1.0948	2.3481 ± 0.8614	2.3479 ± 1.6356	2.0338 ± 0.2648	1.8995 ± 0.3987	2.5622 ± 0.7545	<b>0.8992 ± 0.3583</b>
	600	2.6037 ± 1.1631	2.7002 ± 1.1561	2.5733 ± 1.8155	2.2990 ± 0.1988	2.1915 ± 0.3383	2.7744 ± 0.9136	<b>1.5692 ± 0.3497</b>
	800	2.6638 ± 1.1837	2.9429 ± 1.3532	2.6705 ± 1.8522	2.3862 ± 0.2291	2.3021 ± 0.2791	2.8746 ± 0.9632	<b>1.9195 ± 0.2265</b>
	1000	2.6851 ± 1.1655	3.0044 ± 1.5006	2.7412 ± 1.8404	2.3884 ± 0.1746	2.3194 ± 0.2103	2.8407 ± 0.9803	<b>2.0413 ± 0.1697</b>

**Table 2.** NRMSE for forecasting tasks on real-world datasets ( \* denotes open loop settings).

Dataset	Horizon	NRMSE ↓						
		ESN	SCR	CRJ	SW-ESN	MCI-ESN	DeepESN	HypER
MIT-BIH	200*	2.3520 ± 0.5484	2.0300 ± 0.5225	1.5681 ± 0.3373	1.9976 ± 0.3539	1.1408 ± 0.0604	2.7377 ± 0.9642	<b>0.7412 ± 0.2972</b>
	500*	1.7548 ± 0.3699	1.5411 ± 0.3469	1.2561 ± 0.2130	1.5351 ± 0.2293	1.0512 ± 0.0328	2.0153 ± 0.6588	<b>0.6735 ± 0.2018</b>
	1000*	1.4852 ± 0.2254	1.3715 ± 0.2000	1.2103 ± 0.1132	1.3543 ± 0.1299	1.1262 ± 0.0156	1.6513 ± 0.4127	<b>0.7528 ± 0.1217</b>
Sunspot (monthly)	200*	0.4986 ± 0.0035	0.5626 ± 0.0215	0.5160 ± 0.0068	0.5041 ± 0.0036	<b>0.4870 ± 0.0003</b>	0.4881 ± 0.0092	0.4903 ± 0.0035
	500*	0.3702 ± 0.0021	0.4197 ± 0.0105	0.3825 ± 0.0032	0.3731 ± 0.0020	0.3727 ± 0.0006	<b>0.3647 ± 0.0033</b>	0.3819 ± 0.0052
	1000*	0.3560 ± 0.0028	0.4143 ± 0.0117	0.3833 ± 0.0084	0.3643 ± 0.0049	<b>0.3361 ± 0.0002</b>	0.3562 ± 0.0063	0.3488 ± 0.0033
Santa Fe	200*	0.3014 ± 0.0046	0.3345 ± 0.0203	0.3127 ± 0.0103	0.3043 ± 0.0035	0.3421 ± 0.0018	0.3057 ± 0.0074	<b>0.2853 ± 0.0123</b>
	500*	0.3107 ± 0.0015	0.3196 ± 0.0065	0.3120 ± 0.0036	0.3122 ± 0.0014	0.3260 ± 0.0007	0.3105 ± 0.0026	<b>0.2905 ± 0.0077</b>
	1000*	0.2615 ± 0.0013	0.3046 ± 0.0194	0.2636 ± 0.0069	0.2529 ± 0.0011	0.2737 ± 0.0004	0.2590 ± 0.0040	<b>0.2451 ± 0.0074</b>
Sunspot (monthly)	5	2.7590 ± 0.1903	3.0103 ± 0.6578	2.9065 ± 0.4330	<b>2.5280 ± 0.2193</b>	2.9715 ± 1.0825	2.6047 ± 0.2740	2.5474 ± 0.5361
	10	2.9977 ± 0.2709	2.7096 ± 0.4210	2.4177 ± 0.1901	2.6527 ± 0.3082	2.6360 ± 0.6055	2.4866 ± 0.4580	<b>2.3770 ± 0.5746</b>
	15	3.9134 ± 0.4048	3.3159 ± 0.6076	2.9029 ± 0.2172	3.4978 ± 0.5451	3.0750 ± 0.7089	3.0730 ± 0.7431	<b>2.8761 ± 0.8182</b>
Santa Fe	5	2.0033 ± 0.3560	1.6533 ± 0.3241	<b>1.1579 ± 0.4128</b>	2.0322 ± 0.2692	2.3768 ± 0.1001	1.8717 ± 0.3477	1.4738 ± 0.3298
	10	2.2450 ± 0.4354	1.7234 ± 0.2513	1.7210 ± 0.3957	2.1163 ± 0.2813	2.3586 ± 0.1106	2.1346 ± 0.3688	<b>1.7108 ± 0.3346</b>
	15	2.1451 ± 0.3156	2.1405 ± 0.2713	2.4815 ± 0.9362	2.1235 ± 0.1442	2.1557 ± 0.0746	2.2228 ± 0.2123	<b>1.9747 ± 0.4748</b>

row vectors  $\mathbf{u}_{t+1}$ ,  $\Xi$  stacks the column features  $\xi_t$  and  $I$  is the  $(2N + 1) \times (2N + 1)$  identity matrix. The regularization term  $\lambda I$  ensures that  $\Xi \Xi^T + \lambda I$  is invertible, thus guaranteeing a unique solution, while also penalizing overfitting.

**Operating Protocols.** We start from  $\mathbf{x}_0 = \mathbf{0}$  and iterate the leaky update for  $T_w$  steps to allow transients to decay.

*Teacher forcing:* During training and validation, the true signal  $\mathbf{u}_t$  is injected at every step, so the read-out learns from single-step errors while the reservoir itself remains open-loop and perfectly stabilised.

*Autoregressive forecasting:* For test-time prediction we close the loop, feeding the network’s own output  $\hat{\mathbf{u}}_{t+1} = \mathbf{W}_{\text{out}} \xi_t$  back as the next input. This autonomous mode probes long-horizon fidelity: any geometric or spectral mismatch inside  $W$  accumulates multiplicatively, so gains in Lyapunov-time accuracy translate directly into extended prediction windows.

## 4 Experiments and Discussion

**Setup.** To evaluate the effectiveness of HypER, we conduct a series of experiments on several canonical chaotic systems—standard benchmarks in nonlinear time series modeling—including the butterfly-shaped *Lorenz-63* attractor ( $\lambda_{\max} \approx 0.905$ ) [23], the slower *Rössler* scroll ( $\lambda_{\max} \approx 0.071$ ) [37], the kink-dominated double scroll of *Chua’s circuit* [6], the hyper-chaotic *Chen-Ueta* flow with two positive exponents [5] and the infinite-dimensional delay-differential *Mackey-Glass* system [26]. All benchmark trajectories are generated with the LSODA integrator in SciPy’s `odeint` at a fixed

step size  $\Delta t = 0.02$ , producing 12,500 samples per system. The first 2000 points are discarded as wash-out to mitigate the effects of transient dynamics, the next 80% used for training, and the final 20% reserved for evaluation. Specifically, we integrate the Lorenz ( $\sigma = 10, \rho = 28, \beta = \frac{8}{3}; x_0 = y_0 = z_0 = 1.0$ ), Rössler ( $a = 0.2, b = 0.2, c = 5.7; x_0 = 0.0, y_0 = 1.0, z_0 = 0.0$ ), Chua ( $\alpha = 15.6, \beta = 28, m_0 = -1.143, m_1 = -0.714; x_0 = 0.7, y_0 = z_0 = 0.0$ ) and Chen-Ueta ( $a = 35, b = 3, c = 28; x_0 = y_0 = z_0 = 0.1$ ) systems, parameter regimes that ensure sustained chaotic behaviour in all benchmarks.

We benchmark HypER against several baseline models including ESN [14], SCR [21], CRJ [36], SW-ESN [19], MCI-ESN [22] and DeepESN [10]. All of these are single-reservoir models, except MCI-ESN, which employs two interconnected reservoirs, and DeepESN, which stacks multiple reservoirs in a hierarchical structure. The input weights  $\mathbf{U}$  are drawn from a zero-mean Gaussian distribution clipped to a small symmetric interval, for all models. We instantiate all on equal-footing with 300 units (three 100-unit layers for DeepESN). Global hyperparameters—input weights  $\mathbf{U} \sim \mathcal{N}(0, 0.2^2)$ , spectral radius  $\rho(\mathbf{W}) = 0.99$ , leak rate  $\alpha = 0.8$  and ridge coefficient  $\lambda = 10^{-5}$ —were selected through budgeted hyperparameter search tailored to the Lorenz system; analogous tuning was performed for other datasets. Model-specific hyperparameters were also optimized using the same procedure (*details are laid out in the supplementary file*). All metrics were averaged over 30 independent seeded runs.

**Metrics.** *Normalized Root Mean Squared Error (NRMSE):* We assess the model’s prediction accuracy using NRMSE. Given a true trajectory  $\{\mathbf{u}_t\}_{t=1}^T \subset \mathbb{R}^m$  and a model-predicted trajectory  $\{\hat{\mathbf{u}}_t\}_{t=1}^T$ ,

**Table 3.** Normalized VPT and ADev for autoregressive forecasting over a 1000-step horizon.

Dataset	Model	Norm. VPT $\uparrow$	ADev $\downarrow$
Lorenz	ESN	$5.285 \pm 0.72$	$51.43 \pm 17.56$
	SCR	$5.437 \pm 1.19$	$51.67 \pm 13.29$
	CRJ	$5.558 \pm 0.18$	$43.83 \pm 13.39$
	SW-ESN	$5.927 \pm 0.95$	$35.70 \pm 9.86$
	MCI-ESN	$8.049 \pm 2.36$	$33.50 \pm 14.57$
	DeepESN	$4.883 \pm 1.15$	$54.43 \pm 22.81$
	HypER	<b>12.215 <math>\pm</math> 1.23</b>	<b>19.67 <math>\pm</math> 6.82</b>
Rössler	ESN	$3.442 \pm 1.42$	$4.27 \pm 6.23$
	SCR	$2.857 \pm 1.72$	$7.97 \pm 6.02$
	CRJ	$3.150 \pm 1.15$	$3.03 \pm 1.52$
	SW-ESN	$3.104 \pm 1.17$	$3.10 \pm 1.87$
	MCI-ESN	$3.427 \pm 0.68$	$1.80 \pm 1.52$
	DeepESN	$3.177 \pm 1.35$	$2.10 \pm 1.63$
	HypER	<b>5.142 <math>\pm</math> 0.76</b>	<b>1.27 <math>\pm</math> 1.17</b>
Chen-Ueta	ESN	$2.006 \pm 0.34$	$121.77 \pm 20.48$
	SCR	$1.946 \pm 0.41$	$130.20 \pm 25.69$
	CRJ	$1.934 \pm 0.33$	$101.23 \pm 17.04$
	SW-ESN	$2.107 \pm 0.18$	$104.87 \pm 14.99$
	MCI-ESN	$2.628 \pm 0.44$	$97.57 \pm 14.77$
	DeepESN	$1.635 \pm 0.60$	$138.37 \pm 40.28$
	HypER	<b>5.067 <math>\pm</math> 0.70</b>	<b>80.60 <math>\pm</math> 9.25</b>

**Table 4.** Ablation on manifold geometry, embedding dimension, and—in the Poincaré disc setting—node-sampling strategy (1000-step Lorenz forecasting). Here, ‘Euc. / Uni.’ refers to uniform sampling in Euclidean space; ‘Hyp. / Euc.-Iso’ refers to Euclidean-volume isotropic sampling but in hyperbolic space; ‘Hyp. / Hyp.-Uni.’ refers to uniform sampling in hyperbolic space.

Manifold / Sampling	Dim. $d$	NRMSE $\downarrow$	Norm. VPT $\uparrow$	ADev $\downarrow$
Euc. / Uni.	2	1.3981	11.191	23.13
Hyp. / Euc.-Iso.	2	1.3540	11.947	23.43
Hyp. / Hyp.-Uni.	2	<b>1.2580</b>	<b>12.215</b>	<b>19.67</b>
Hyp. / Hyp.-Uni.	3	1.3702	11.192	21.37
Hyp. / Hyp.-Uni.	4	1.4639	10.817	22.03

**Table 5.** Performance comparison of models on the Lorenz dataset using mixed heterogeneous node-wise activation functions. MCI-ESN is excluded as its built-in complementary sine-cosine activations preclude a fair comparison.

Model	NRMSE $\downarrow$	Norm. VPT $\uparrow$	ADev $\downarrow$
ESN	1.9436	5.933	42.57
SCR	1.7270	7.086	32.30
CRJ	1.6718	7.423	31.97
SW-ESN	1.4974	9.636	26.20
DeepESN	2.0225	5.257	40.53
HypER	<b>1.2580</b>	<b>12.215</b>	<b>19.67</b>

**Table 6.** Ablation over HypER parameters (1000-step autoregressive forecasting of the Lorenz dataset).

Parameter	Setting	NRMSE $\downarrow$	Norm. VPT $\uparrow$	ADev $\downarrow$
Kernel Width	$\sigma = 0.05$	1.3421	12.052	24.57
	$\sigma = 0.1$	<b>1.2580</b>	<b>12.215</b>	<b>19.67</b>
	$\sigma = 0.2$	1.3311	12.101	20.87
	$\sigma = 0.3$	1.3668	11.591	23.63
	$\sigma = 0.5$	1.4257	11.524	23.60
Row-level Sparsity	$\kappa = 10$	1.2827	12.210	19.77
	$\kappa = 20$	1.2923	12.211	20.67
	$\kappa = 40$	<b>1.2580</b>	<b>12.215</b>	<b>19.67</b>
	$\kappa = 60$	1.2665	12.213	18.67
	$\kappa = 80$	1.2761	12.212	<b>17.70</b>

the NRMSE is defined as  $\sqrt{\frac{\sum_{t=1}^T \|\mathbf{u}_t - \hat{\mathbf{u}}_t\|^2}{\sum_{t=1}^T \|\mathbf{u}_t - \bar{\mathbf{u}}\|^2}}$ .

*Valid Prediction Time (VPT):* To quantify long-horizon accuracy

in a chaotic setting, we compute *valid prediction time*  $T_{\text{VPT}}$  as follows. We first define the time-averaged variance of  $\mathbf{u}_t$  by centering about its mean  $\bar{\mathbf{u}} \in \mathbb{R}^m$  and computing  $\langle \|\mathbf{u}_t - \bar{\mathbf{u}}\|^2 \rangle$  over the entire prediction horizon. Next, we define the *normalized prediction error* at time  $t$  by  $\delta(t) = \frac{\|\mathbf{u}_t - \hat{\mathbf{u}}_t\|^2}{\langle \|\mathbf{u}_t - \bar{\mathbf{u}}\|^2 \rangle}$ . For a task-specific threshold  $\theta$  (we use  $\theta = 0.4$  [32]),  $T_{\text{VPT}}$  is the earliest time  $t$  at which  $\delta_t$  exceeds  $\theta$ . If  $\delta_t \leq \theta$  for all  $t$ , then  $T_{\text{VPT}}$  is taken to be the final available time. Finally, to relate  $T_{\text{VPT}}$  to the system’s characteristic divergence, we introduce the *Lyapunov time*  $T_L = 1/\lambda_{\max}$ , where  $\lambda_{\max} > 0$  is the LLE. The ratio  $\frac{T_{\text{VPT}}}{T_L}$  indicates how many Lyapunov  $e$ -foldings the model’s predictions remain within the acceptable error threshold.

*Attractor Deviation (ADev):* To measure how well the predicted trajectory resembles the true one in phase-space, we partition the domain into a uniform grid of  $N_x \times N_y \times N_z$  cubes [41]. For each cube  $(i, j, k)$  we record an occupancy indicator  $\chi_{ijk}^{\text{true}}, \chi_{ijk}^{\text{pred}} \in \{0, 1\}$ , equal to 1 if the true (respectively predicted) trajectory visits that cube at least once during the prediction window and 0 otherwise. The *attractor deviation* is then  $\text{ADev} = \sum_{i=1}^{N_x} \sum_{j=1}^{N_y} \sum_{k=1}^{N_z} |\chi_{ijk}^{\text{true}} - \chi_{ijk}^{\text{pred}}|$ . ADev counts the number of cubes that are visited by exactly one of the two trajectories (the symmetric-difference volume). ADev = 0 indicates perfect geometric agreement, whereas larger values reflect mismatch.

*Power Spectral Density (PSD):* While previous evaluation metrics assessed the models from a time-domain perspective, we now turn to a *frequency-domain analysis* to evaluate how well the reconstructed trajectory preserves the spectral characteristics of the true signal. Specifically, we examine PSD of each component of the trajectory using *Welch’s Method*. Initially, a *Hamming Window*  $w_k$  is applied to the discrete signal  $z_k = \mathbf{z}(k \Delta t)$  to minimize spectral leakage by tapering the edges of the signal. The PSD is then computed as the squared magnitude of the *Fast Fourier Transform (FFT)* of the windowed signal  $z_k \cdot w_k$ , averaged over all segments  $S(\omega) = \mathbb{E} [|\mathcal{F}\{z_k \cdot w_k\}|^2]$ .

**Datasets.** Our real-world testbed spans three orders of temporal scale. The *Sunspot Monthly* series provides a 270-year, quasi-periodic benchmark whose Schwabe and Gleissberg modulations have long served as a litmus for nonlinear predictors; we standardise the SILSO v2.0 index and withhold the last 84 years for out-of-sample scoring [40], we use the first 4,500 samples for training and the following 1,000 for testing in our forecasting setup [16, 34]. Biomedical variability is probed with the *MIT-BIH Arrhythmia* corpus, where 48 annotated ECG records sampled at 360 Hz are partitioned 80/20; this sequence mixes quasi-periodic sinus segments with abrupt ectopic events, stressing robustness to morphological outliers [12, 28]. The aforesaid datasets are normalized to the  $[0, 1]$  range and processed using 3-dimensional delay embedding prior to training. (*details in supplementary*)

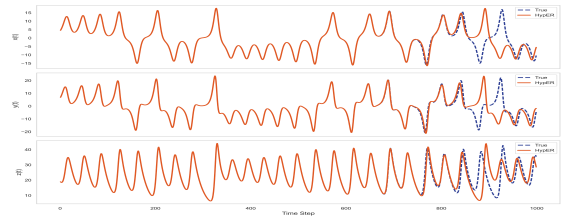


**Figure 3.** Predicted trajectories by HypER alongside ground truth for the test segment of the Lorenz system under autoregressive forecasting.

**Results.** On chaotic testbeds (Table 1), for Lorenz-63, NRMSE increases rapidly with horizon for all Euclidean reservoirs, exceed-

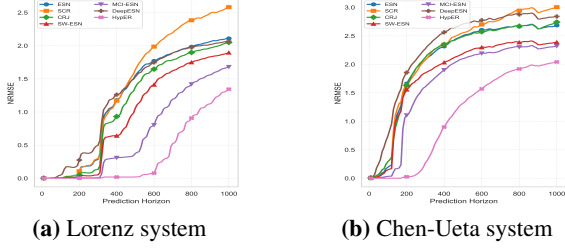


**Figure 4.** NRMSE for autoregressive predictions across multiple horizons.

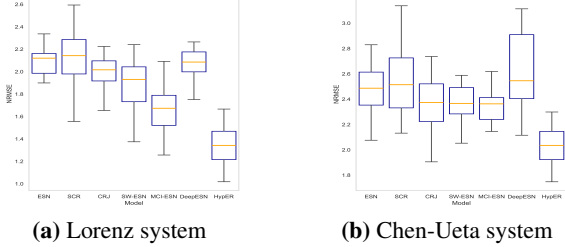


**Figure 5.** Boxplots of NRMSE for autoregressive predictions at a 1000-step prediction horizon.

ing one (fully de-correlated forecasts) after  $\sim 6T_L$ . By contrast HyperER holds sub-percent error out to 800 steps on Lorenz (cf. Fig. 3) and keeps NRMSE one order of magnitude lower than the next best model on Rössler at every horizon, confirming that the hyperbolic expansion factor  $\beta(\sigma) > 1$  indeed delays error amplification. Even on the stiff hyper-chaotic Chen-Ueta attractor (cf. Figs. 4, 5), where all baselines saturate near the aperiodic variance floor, HyperER cuts long-horizon error by  $\approx 12\%$  at 1000 steps, validating the theoretical claim that negative curvature raises the minimum Jacobian gain while preserving ESP. As Fig. 6 shows, HyperER retains the true Lorenz power spectrum, whereas the standard ESN spectrum collapses into spurious high-frequency noise.

On real-world data (Table 2), in fully open-loop cardiac benchmarks, HyperER cuts the best baseline NRMSE by  $\approx 35\%$  at every horizon, showing that geometric bias translates beyond synthetic flows. On smoother solar-cycle data, the advantage disappears, aligning with theory: when the generator is quasi-periodic rather than chaotic, enlarging  $\lambda_{\min}(W)$  is unnecessary, so hyperbolic wiring behaves like a neutral prior. Overall, the tables demonstrate that HyperER’s curvature-controlled expansion preserves ESP yet provides exploitable separation exactly where standard reservoirs struggle. On the highly non-stationary Santa Fe series, HyperER outperforms the nearest Euclidean reservoir by roughly 7% across closed-loop horizons, indicating that its curvature-induced expansion remains beneficial even in noisy, broadband experimental chaos.

Across all three chaotic benchmarks, HyperER lifts the normalised VPT far beyond every Euclidean reservoir (Table 3), enlarging the window of trajectory fidelity by roughly +49% on Rössler, +52% on Lorenz, and a full  $2\times$  on the stiff Chen-Ueta flow. At the same time it slashes ADev by 41% on Lorenz and about one-third on Rössler, while still shaving almost 17% off the Chen baseline. These dual gains confirm the theoretical picture: the curvature-controlled lower bound on the Jacobian’s smallest singular value extends the period during which closed-loop dynamics track the true attractor, and the concomitant drop in ADev shows that this stability is achieved without sacrificing pointwise spatial accuracy. (*Results for open-loop setting are presented in the supplementary file.*)

**Ablation.** Holding reservoir size fixed (Table 4), moving from a flat Euclidean lattice to the Poincaré disc cuts 1000-step NRMSE

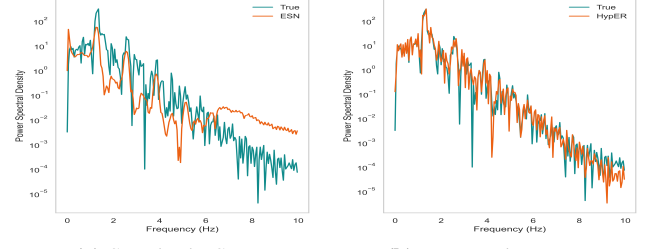


**Figure 6.** PSD plots of autoregressive predictions at a 1000-step horizon when both networks are driven by the Lorenz system.

by 3% even when the nodes are still placed with Euclidean-volume sampling; switching to *hyperbolic-uniform* sampling supplies the full curvature bias and yields an additional 7% drop in error together with the best VPT and ADev. Increasing the latent dimension beyond the disc (to  $d = 3, 4$ ) weakens these gains, confirming the theorem’s prediction that the Jacobian expansion factor  $\beta(\sigma)$  is maximised when curvature is concentrated rather than spread over extra dimensions.

Replacing a homogeneous tanh reservoir by a tanh-sine-linear mix lifts every Euclidean baseline (Table 5) but lifts HyperER most: its NRMSE is 16% lower, and VPT is 27% higher than the best graph-structured ESN (a ReLU variant is included for ablation). This indicates that the curvature-induced amplification preserves the diverse nonlinear signatures instead of letting them collapse under ESP constraints. The kernel width  $\sigma$  shows a clear optimum around 0.1; narrower kernels ( $\sigma < 0.05$ ) under-connect the graph and reduce VPT (Table 6), while wider kernels dilute curvature and push  $\beta(\sigma)$  back toward unity. Row-level sparsity  $\kappa$  is broad-tolerant: performance plateaus between 40 – 80 neighbours, with denser reservoirs slightly improving ADev but not NRMSE, confirming that HyperER’s advantages arise from geometry rather than sheer connectivity.

**Computational Footprint.** HyperER sidesteps manifold optimization by fixing reservoir weights and training only the read-out. Constructing the adjacency matrix costs  $O(N^2)$  but reduces to  $O(\kappa N)$  under sparsity, yielding 300-node reservoirs that build in  $<15$  s on an A100 GPU with only 48 KB memory.

## 5 Conclusion

We introduced an RC framework—HYPER—that operates on a negatively curved manifold to capture the exponential divergence inherent in chaotic systems. By mapping reservoir nodes into the Poincaré ball, we explicitly encode geometric properties that mirror the local “stretch-and-fold” mechanism typical of chaos. Through both theoretical motivation and empirical evaluation on benchmark chaotic systems, we have shown that endowing the reservoir with hyperbolic geometry can extend valid prediction horizons beyond what is typically achievable with Euclidean or topologically random reservoirs.

Several important directions remain open for further research. First, while we have focused on select chaotic attractors, other higher-dimensional flows or spatiotemporal PDEs may exhibit additional structures that can benefit from more general hyperbolic embeddings or layer-by-layer manifold compositions. Second, more sophisticated sampling schemes—such as adaptive node placement or non-uniform radial distributions—could enhance the reservoir’s ability to capture specific dynamical modes within highly complex attractors. Third, integrating modern RC extensions (e.g., output feedback, hierarchical readouts, or online adaptation) might further improve long-horizon stability. Finally, exploring systematic links between Lyapunov exponents and the negative curvature parameter of

fers a potential route to tailor the reservoir's geometry to specific tasks.

## References

- [1] J. W. Anderson. *Hyperbolic Geometry*. Springer, London, 1999. ISBN 978-3540660880. Geodesic characterisation of the Poincaré ball; see Ch. 2, Prop. 2.2.
- [2] D. V. Buonomano and M. D. Mauk. Neural network model of the cerebellum: Temporal discrimination and the timing of motor responses. *Neural Computation*, 6(1):38–55, 1994. doi: 10.1162/neco.1994.6.1.38.
- [3] T. L. Carroll. Optimizing memory in reservoir computers. *Chaos: An Interdisciplinary Journal of Nonlinear Science*, 32(2):023123, 02 2022. ISSN 1054-1500. doi: 10.1063/5.0078151.
- [4] I. Chami, R. Ying, C. Re, and J. Leskovec. Hyperbolic graph convolutional neural networks. In *Proceedings of the 33rd International Conference on Neural Information Processing Systems (NeurIPS)*, Red Hook, NY, USA, 2019. Curran Associates Inc.
- [5] G. Chen and T. Ueta. Yet another chaotic attractor. *International Journal of Bifurcation and Chaos*, 9(07):1465–1466, 1999.
- [6] L. Chua, M. Komuro, and T. Matsumoto. The double scroll family. *IEEE Transactions on Circuits and Systems*, 33(11):1072–1118, 1986.
- [7] M. P. do Carmo. *Riemannian Geometry: Theory & Applications*. Birkhäuser, Boston, 1992. ISBN 978-0817634902. Graduate Texts in Mathematics, Vol. 176.
- [8] J. P. Eckmann and D. Ruelle. Ergodic theory of chaos and strange attractors. *Rev. Mod. Phys.*, 57:617–656, Jul 1985. doi: 10.1103/RevModPhys.57.617.
- [9] H. Fan, J. Jiang, C. Zhang, X. Wang, and Y.-C. Lai. Long-term prediction of chaotic systems with machine learning. *Phys. Rev. Res.*, 2: 012080, Mar 2020. doi: 10.1103/PhysRevResearch.2.012080.
- [10] C. Gallicchio and A. Micheli. Deep Echo State Network (DeepESN): A Brief Survey. *arXiv*, 12 2017. doi: 10.48550/arXiv.1712.04323.
- [11] O. Ganea, G. Becigneul, and T. Hofmann. Hyperbolic neural networks. In S. Bengio, H. Wallach, H. Larochelle, K. Grauman, N. Cesa-Bianchi, and R. Garnett, editors, *Advances in Neural Information Processing Systems (NeurIPS)*, volume 31. Curran Associates, Inc., 2018.
- [12] A. L. Goldberger, L. A. N. Amaral, L. Glass, J. M. Hausdorff, P. C. Ivanov, R. G. Mark, J. E. Mietus, G. B. Moody, C.-K. Peng, and H. E. Stanley. Physiobank, physiotoolkit, and physionet: Components of a new research resource for complex physiologic signals. *Circulation*, 101(23):e215–e220, June 2000. doi: 10.1161/01.CIR.101.23.e215.
- [13] J. J. Hopfield. Neural networks and physical systems with emergent collective computational abilities. *Proceedings of the National Academy of Sciences (PNAS)*, 79(8):2554–2558, 1982.
- [14] H. Jaeger. The “Echo State” Approach to Analysing and Training Recurrent Neural Networks. *GMD Technical Report*, 148:1–47, 2001.
- [15] H. Jaeger and H. Haas. Harnessing Nonlinearity: Predicting Chaotic Systems and Saving Energy in Wireless Communication. *Science*, 304 (5667):78–80, 2004. doi: 10.1126/science.1091277.
- [16] H. Jaeger, M. Lukosevicius, D. Popovici, and U. Siewert. Optimisation and applications of echo state networks with leaky-integrator neurons. *Neural Networks*, 20(3):335–352, 2007.
- [17] L. Jaurigue. Chaotic attractor reconstruction using small reservoirs—the influence of topology. *Machine Learning: Science and Technology*, 5(3):035058, aug 2024. doi: 10.1088/2632-2153/ad6ee8.
- [18] A. Katok and B. Hasselblatt. *Introduction to the Modern Theory of Dynamical Systems*. Cambridge University Press, Cambridge, 1995.
- [19] Y. Kawai, J. Park, and M. Asada. A small-world topology enhances the echo state property and signal propagation in reservoir computing. *Neural Networks*, 112:15–23, 2019. doi: 10.1016/j.neunet.2018.12.012.
- [20] J. M. Lee. *Introduction to Riemannian Manifolds*. Springer, New York, 2 edition, 2018. ISBN 978-3319917542. Graduate Texts in Mathematics, Vol. 176.
- [21] B. Li, R. S. Fong, and P. Tiño. Simple cycle reservoirs are universal. *Journal of Machine Learning Research (JMLR)*, 25(1), Jan. 2024. ISSN 1532-4435.
- [22] J. Liu, X. Xu, and E. Li. A minimum complexity interaction echo state network. *Neural Computing and Applications*, 36:4013–4026, 2024. doi: 10.1007/s00521-023-09271-9.
- [23] E. N. Lorenz. Deterministic nonperiodic flow. *Journal of the Atmospheric Sciences*, 20(2):130–141, 1963.
- [24] Z. Lu, J. Pathak, B. Hunt, M. Girvan, and E. Ott. Reservoir observers: Model-free inference of unmeasured variables in chaotic systems. *Chaos*, 27(4):041102, 2017. doi: 10.1063/1.4979665.
- [25] W. Maass, T. Natschlager, and H. Markram. Real-Time Computing Without Stable States: A New Framework for Neural Computation Based on Perturbations. *Neural Computation*, 14(11):2531–2560, 2002.
- [26] M. Mackey and L. Glass. Oscillation and chaos in physiological control systems. *Science (New York, N.Y.)*, 197:287–9, 08 1977. doi: 10.1126/science.267326.
- [27] V. Mante, D. Sussillo, K. V. Shenoy, and W. T. Newsome. Context-dependent computation by recurrent dynamics in prefrontal cortex. *Nature*, 503(7474):78–84, 2013.
- [28] G. B. Moody and R. G. Mark. The impact of the mit-bih arrhythmia database. *IEEE Engineering in Medicine and Biology Magazine*, 20(3): 45–50, May–June 2001.
- [29] M. Nickel and D. Kiela. Poincaré embeddings for learning hierarchical representations. In *Proceedings of the 31st International Conference on Neural Information Processing Systems, NIPS’17*, page 6341–6350, Red Hook, NY, USA, 2017. Curran Associates Inc. ISBN 9781510860964.
- [30] A. Ohkubo and M. Inubushi. Reservoir computing with generalized readout based on generalized synchronization. *Nature Scientific Reports*, 14:30918, 2024. doi: 10.1038/s41598-024-81880-3.
- [31] T. N. Palmer. *Predictability of weather and climate: from theory to practice*, page 1–29. Cambridge University Press, 2006.
- [32] J. Pathak, B. Hunt, M. Girvan, Z. Lu, and E. Ott. Model-free prediction of large spatiotemporally chaotic systems from data: A reservoir computing approach. *Physical Review Letters*, 120(2):024102, 2018. doi: 10.1103/PhysRevLett.120.024102.
- [33] J. Pathak, A. Wikner, R. Fussell, S. Chandra, B. R. Hunt, M. Girvan, and E. Ott. Hybrid forecasting of chaotic processes: Using machine learning in conjunction with a knowledge-based model. *Chaos: An Interdisciplinary Journal of Nonlinear Science*, 28(4):041101, 04 2018. ISSN 1054-1500. doi: 10.1063/1.5028373.
- [34] D. R. Rigney, A. L. Goldberger, W. C. Ocasio, Y. Ichimaru, G. B. Moody, and R. G. Mark. Multi-channel physiological data: description and analysis. In A. S. Weigend and N. A. Gershenfeld, editors, *Time Series Prediction: Forecasting the Future and Understanding the Past*, pages 105–129. Addison-Wesley, Reading, MA, 1993.
- [35] A. Rodan and P. Tino. Minimum complexity echo state network. *IEEE Transactions on Neural Networks*, 22(1):131–144, Jan 2011. doi: 10.1109/TNN.2010.2089641.
- [36] A. Rodan and P. Tino. Simple deterministically constructed cycle reservoirs with regular jumps. *Neural computation*, 24(7):1822–1852, 2012.
- [37] O. E. Rössler. An equation for continuous chaos. *Physics Letters A*, 57 (5):397–398, 1976.
- [38] H. S. Seung. How the brain keeps the eyes still. *Proceedings of the National Academy of Sciences (PNAS)*, 93(23):13339–44, 1996.
- [39] W. P. Thurston. *Three-Dimensional Geometry and Topology. Vol. 1*. Princeton University Press, Princeton, 1997. ISBN 978-0691084213.
- [40] B. World Data Center SILSO, Royal Observatory of Belgium. World data center silso, Royal Observatory of Belgium, Brussels. <http://sidc.be/silso/datafiles>, 2020. Version 2.0, monthly mean total sunspot number, accessed 2025-04-01.
- [41] Z.-M. Zhai, L.-W. Kong, and Y.-C. Lai. Emergence of a resonance in machine learning. *Physical Review Research*, 5(3):033127, 2023. doi: 10.1103/PhysRevResearch.5.033127.
- [42] H. Zhang, P. D. Rich, A. K. Lee, and T. O. Sharpee. Hippocampal spatial representations exhibit a hyperbolic geometry that expands with experience. *Nature Neuroscience*, 26(1):131–139, Jan 2023. doi: 10.1038/s41593-022-01212-4. Epub 2022 Dec 29.